

**Submonolayers of carbon on  $\alpha$ -Fe facets: An *ab initio* study**S. Riikonen,<sup>1,2</sup> A. V. Krasheninnikov,<sup>1,3</sup> and R. M. Nieminen<sup>1,\*</sup><sup>1</sup>*COMP/Department of Applied Physics, Aalto University School of Science and Technology,  
P.O. Box 11000, FI-00076 Aalto, Espoo, Finland*<sup>2</sup>*Laboratory of Physical Chemistry, Department of Chemistry, University of Helsinki, P.O. Box 55, FI-00014, Helsinki, Finland*<sup>3</sup>*Department of Physics, University of Helsinki, P.O. Box 43, FI-00014, Helsinki, Finland*

(Received 7 June 2010; revised manuscript received 26 August 2010; published 30 September 2010)

Motivated by recent *in situ* studies of carbon nanotube growth from large transition-metal nanoparticles, we study various  $\alpha$ -iron (ferrite) facets at different carbon concentrations using *ab initio* methods. The studied (110), (100), and (111) facets show qualitatively different behavior when carbon concentration changes. In particular, adsorbed carbon atoms repel each other on the (110) facet, resulting in carbon dimer and graphitic material formation. Carbon on the (100) facet forms stable structures at concentrations of about 0.5 monolayer and at 1.0 monolayer this facet becomes unstable due to a frustration of the top-layer iron atoms. The stability of the (111) facet is weakly affected by the amount of adsorbed carbon and its stability increases further with respect to the (100) facet with increasing carbon concentration. The exchange of carbon atoms between the surface and subsurface regions on the (111) facet is easier than on the other facets and the formation of carbon dimers is exothermic. These findings are in accordance with a recent *in situ* experimental study where the existence of graphene-decorated (111) facets is related to increased carbon concentration.

DOI: [10.1103/PhysRevB.82.125459](https://doi.org/10.1103/PhysRevB.82.125459)

PACS number(s): 81.16.Hc, 31.15.A–, 81.07.De, 68.43.–h

**I. INTRODUCTION**

Carbon nanotubes (CNTs) are a versatile material with a wide range of potential technological applications in fields such as mechanical engineering, electronics and biotechnology. The chemical vapor deposition (CVD) method has established itself as the most effective way to produce CNTs in mass quantities. In this method, carbon containing molecules (hydrocarbons, CO) are dissociated on catalytic nanoparticles (typically transition metals and their alloys) where carbon eventually forms graphitic structures and nanotubes. For wider technological exploitation of CNTs, better control over the growth process is needed. Controlling nanotube chirality and preventing particle poisoning and CNT growth termination are the most important aspects. In order to gain such a control, insight at microscopic level into the CNT growth process is needed. This kind of insight can be obtained by performing *in situ* experiments where the CNT growth is directly observed.

Recently, several *in situ* environmental transmission-electron microscopy (TEM) studies of carbon fiber and nanotube growth have been carried out.<sup>1–10</sup> In these studies, the catalyst particles were either crystalline and/or “liquidlike” (i.e., crystalline with high self-diffusivity) during the growth process. Studied nanoparticle materials ranged from nickel,<sup>2,3,5,9</sup> cobalt,<sup>4,7,9</sup> and iron<sup>6,7</sup> to alloys<sup>7</sup> of these metals. A common factor in many of these investigations is the appearance of step edges and new facets as carbon is introduced to the nanoparticle and the growth of graphene layers from these special regions.<sup>2,5–7</sup> In the case of nickel, this phenomenon was attributed to the stabilization of nanoparticle step edges upon carbon adsorption and the transport of catalyst metal atoms away from the step-edge region.<sup>2,5,11</sup> The energy barrier for carbon bulk diffusion in nickel was concluded to be very high when compared to any surface related diffusion phenomena.<sup>5</sup>

In several studies, the dominant role of surface and subsurface has been emphasized<sup>3–5</sup> while other studies, considering mainly iron, suggest the important role of bulk diffusion.<sup>7,9,12</sup> Very recently, CNT growth from carbidic phase (cementite) in iron nanoparticles has been observed.<sup>8,10</sup>

In a very recent study, solid-state  $\alpha$ -iron nanoparticle was encapsulated inside multiwalled carbon nanotubes (MWCNTs) while carbon was injected into the nanoparticle by electromigration.<sup>6</sup> The nanoparticle was observed to stay solid and crystalline during the growth. Similar to earlier *in situ* studies, new facets, showing growth of graphitic material, appeared on the nanoparticle surface. The orientation of the nanoparticle was analyzed and the MWCNT walls encapsulating the nanoparticle were parallel to the (110) facet. The existence of the (111) facet was observed to depend strongly on carbon concentration, and nanotube cap was formed on a rounded (100) facet. *Ab initio* simulations were performed for “graphenated” and carbon saturated surfaces in order to reproduce the nanoparticle shape.<sup>6</sup>

In the case of  $\alpha$ -iron, the morphology of (110), (100), and (111) facets is quite different. This can result in very different diffusion barriers, carbon-carbon bond formation energetics and kinetics. For better understanding of experiments it is important to perform *ab initio* simulations and correlate computational results to the phenomena observed in the *in situ* studies. In particular, surface energies can be used to produce the physical shape of the nanoparticle which can be compared with the experiments.<sup>6,13</sup> Activation energies of diffusion on and into the facets may provide information about rate-limiting steps of graphitic material formation.<sup>5,14</sup>

Recently, there have been several *ab initio* studies related to these issues: pure  $\alpha$ -iron facets have been studied extensively by Błóński and Kiejna<sup>15,16</sup> while carbon adsorption and diffusion on and into the (110) and (100) facets were studied by Jiang and Carter.<sup>17</sup> The (100) facet has drawn some attention very recently, as segregated carbon atoms

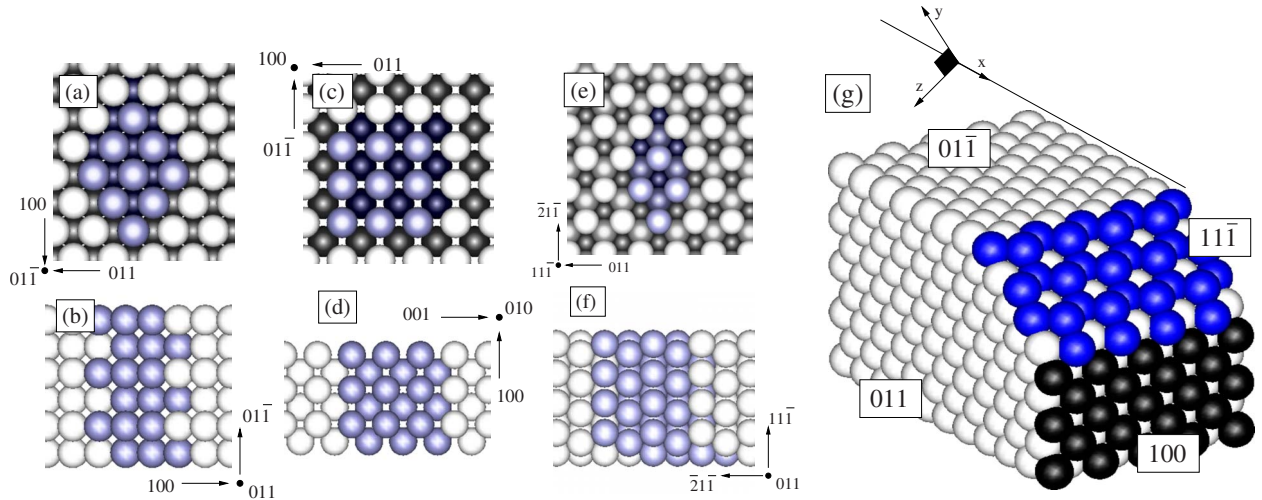


FIG. 1. (Color online) Computational unit cells for different  $\alpha$ -iron surfaces used in the simulations viewed from (a,c,e) top and from (b,d,f) side. [(a) and (b)] (110), [(c) and (d)] (100), and [(e) and (f)] (111) surfaces. Atoms in topmost (lowermost) layers are marked with brighter (darker) shades. Atoms in the unit cells used in this work are marked with blue color. For (110) and (100) the unit cells correspond to  $3 \times 3$  periodicity while for (111) to  $2 \times 2$  periodicity. (g) A portion of bulk  $\alpha$ -iron cut at different angles, demonstrating the relative positions of different surfaces. For (100) surface, the topmost layer is marked with black color. For (111) surface, the two topmost layers are marked with blue color.

form stable, periodic structures on this facet.<sup>18–21</sup> Carbon diffusion and adsorption up to 2 monolayer (ML) concentration on this facet has been studied in detail by Sorescu.<sup>22</sup> Also several cementite surfaces have been studied with *ab initio* methods by Chiou and Carter.<sup>23</sup>

In this work we study the  $\alpha$ -iron (110), (100), and (111) facets at different carbon concentrations. We address such topics as the interaction of adsorbate atoms in coadsorption configurations, carbon diffusion [for the (111) facet] and formation of stable carbon-rich structures [mainly on the (100) facet] in the topmost iron layer. Relative surface energies as function of carbon concentration and energetics of the smallest units involved in graphitic growth, the  $C_2$  molecules, are studied. This work is organized as follows: in Sec. II, simulation of iron-carbon systems, different carbon chemical potentials, calculation of surface energies and computational details are discussed. In Sec. III the morphology of the studied  $\alpha$ -iron facets is discussed followed by the computational results. Discussions and conclusions are made in Sec. IV.

## II. METHODS

### A. Iron-carbon systems

Iron with dissolved carbon exhibits a rich phase diagram as a function of temperature and carbon concentration, where  $\alpha$ -iron (“ferrite,” bcc crystalline, ferromagnetic),  $\gamma$ -iron (“austenite,” fcc crystalline, antiferromagnetic) and cementite ( $Fe_3C$ ) are among the competing phases.<sup>24,25</sup> When considering nanoparticles instead of bulk, the phase diagram will be modified; in particular, it is known that small iron nanoparticles prefer the  $\gamma$ -iron phase instead of the bulk  $\alpha$ -iron phase.<sup>26,27</sup>

While collinear spin calculations within the density-functional theory (DFT) and generalized gradient approximation (GGA) (Ref. 28) seem to work very well for  $\alpha$ -iron,<sup>29</sup>

it is not obvious how to perform calculations for  $\gamma$ -iron, as this phase is observed typically at high temperatures and it is paramagnetic. These and some other problems have been discussed in detail by Jiang and Carter in Ref. 29.

Considering systems involving nanoparticles, it has been shown that “large” iron nanoparticles (more than  $\approx 100$  atoms) prefer the bcc structure.<sup>26</sup> This structure was also observed in the large iron nanoparticle investigated in the recent *in situ* experimental study.<sup>6</sup>

### B. Technical details

In order to visualize the different  $\alpha$ -iron facets, a small volume of bulk, cleaved into several directions is illustrated in Fig. 1(g). The form of this bulk volume mimics the elongated nanoparticles seen in the *in situ* experiment.<sup>6</sup> A real nanoparticle has of course, several other facets which are not visualized in Fig. 1(g) and not considered in this work. Top and side views of the facets are illustrated in panels (a)–(f) of Fig. 1.

We employ the periodic supercell method to model the iron facets. An infinite surface is modeled by a slab consisting of few layers of iron atoms with sufficient vacuum (15 Å) between the slabs. The slabs we have used are depicted in Fig. 1 and they consist of  $3 \times 3 \times 6$  (the last number denoting the number of layers) and  $2 \times 2 \times 12$  slabs for (110), (100), and (111) surfaces, respectively. Areas of the unit cells depicted in Fig. 1 are  $51 \text{ \AA}^2$ ,  $72 \text{ \AA}^2$ , and  $56 \text{ \AA}^2$  for (110), (100), and (111) slabs, respectively. The (110) and (100) unit cells contain 54 iron atoms while the (111) unit cell has 48 iron atoms.

Next, in order to calculate adsorption and reaction energies on the surface, we define a convenient energy quantity  $E_s$  (shifted energies) as follows:

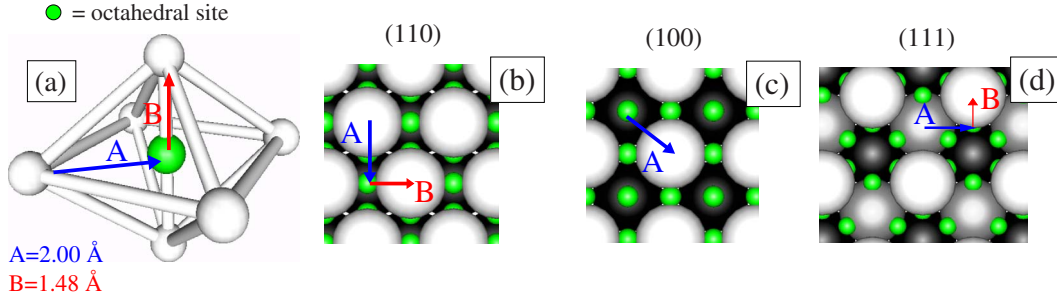


FIG. 2. (Color online) Local coordination at the bulk octahedral site in  $\alpha$ -iron and how it is exposed on the (110), (100), and (111) facets. The octahedral site is marked in all insets with green color. (a) The coordination of octahedral site in the bulk. Exposed bulk octahedral sites on the (b) (110), (c) (100), and (d) (111) facets.

$$E_s(X^*) = E(X^*) - E_0, \quad (1)$$

where  $E(X^*)$  is the energy of the adsorbed surface species  $X^*$  and  $E_0$  is the energy of a surface unit cell without adsorbates. Now the adsorption energy can be written as follows:

$$E_{ads} = E(X^*) - E(X) - E_0 = E_s(X^*) - E(X), \quad (2)$$

where  $E(X)$  is the energy of an isolated atom in vacuum.

We also present adsorption energies, especially in the case of high carbon coverage, with some other chemical potential

$$E_c = E(X^*) - (E_0 + n\mu_c) = E_s(X^*) - n\mu_c, \quad (3)$$

where  $n$  is the number of carbon atoms and  $\mu_c$  is the chemical potential. We take the chemical potential as the energy per atom in graphene. Energy  $E_c$  then reflects the energy cost to accommodate carbon atoms into the metal adsorbent instead of graphene. In previous works<sup>6,20,29</sup> various chemical potentials have been used, including the energy per isolated carbon atom and the energy per carbon atom in graphite or in graphene.

The shifted energy values of Eq. (1) can be used to calculate reaction energetics on the adsorbent, i.e., to look at energetics of processes like  $C^* + C^* \rightarrow C_2^*$ . The energy for a reaction  $X^* + Y^* \rightarrow XY^*$  can be calculated as follows:

$$\Delta E = [E(XY^*) + E_0] - [E(X^*) + E(Y^*)]. \quad (4)$$

This equation can be written, using the energy values  $E_s$  of Eq. (1) as follows:

$$\Delta E = E_s(XY^*) - [E_s(X^*) + E_s(Y^*)]. \quad (5)$$

In the Results section, we tabulate values of  $E_s$  and then use these tabulated values to calculate reaction energetics  $X^* + Y^* \rightarrow XY^*$  using Eq. (5).

The surface energy  $G$  of a specific nanoparticle facet with adsorbates has in some earlier works<sup>6,30</sup> been defined as follows:

$$G = E(X^*) - NE^{bulk} - n\mu_c, \quad (6)$$

where  $N$  is the number of the surface atoms in the slab used for simulations and  $E^{bulk}$  is the energy per atom in the bulk. As Eq. (6) reflects the energy cost to create a surface from the bulk and adsorbing atoms on the surface, it is more accurate to use an equation involving explicitly the surface energy  $E_{surf}$  as follows:

$$G = E_{surf} + E_c, \quad (7)$$

where  $E_c$  is the adsorption energy of Eq. (3). In Eq. (7) the surface energy  $E_{surf}$  is a well defined quantity while the chemical potential of the carbon adsorbates is sensitive to the source of carbon atoms.

In this work we use the values calculated by Blónski and Kijena<sup>15,16</sup> for the (110), (100), and (111) facets which have been evaluated as discussed by Boettger.<sup>31</sup> These are  $E_{surf} = 140 \text{ meV}/\text{\AA}^2$  for the Fe(110) and Fe(100) surfaces and  $E_{surf} = 160 \text{ meV}/\text{\AA}^2$  for the Fe(111) surface.<sup>16</sup>

Our calculations were performed in the framework of the DFT, as implemented in the VASP code.<sup>32,33</sup> All calculations were done using projector-augmented waves<sup>34</sup> and the Perdew-Burke-Ernzerhof GGA exchange correlation functional.<sup>28</sup> We used the Monkhorst-Pack sampling<sup>35</sup> of the Brillouin zone in calculations involving the slab. The sampling used was  $7 \times 7 \times 1$  in the case of all the slabs which corresponds to  $A_{BZ} \approx 0.01 \text{ \AA}^{-2}$  (area in the reciprocal space per sampled  $k$  point). A systematic search to find the optimal adsorption sites for C atoms and  $C_2$  molecules was performed on the slabs of Fig. 1 along the lines of Ref. 36.

Spin polarization was included in all calculations. The cut-off energy of the plane wave basis set was always 420 eV. The mixing scheme in the electronic relaxation was the Methfessel-Paxton method<sup>37</sup> of order 1. Conjugate-gradient relaxation of the geometry was performed and if needed, the relaxation was continued with a semi-Newton scheme. This way we were able to reach a maximum force residual of  $\approx 0.01 \text{ eV}/\text{\AA}$ . In all calculations the special Davidson block iteration scheme was used and symmetries of the adsorption geometries were not utilized.

As carbon chemical potential, we used either the energy of an isolated atom in vacuum or the energy per atom in graphene. For calculation of the chemical potential, identical parameters to those described earlier in this section were used. For an isolated, spin-polarized carbon atom calculated in a cubic unit cell with 15  $\text{\AA}$  sides, we obtained the total energy of  $E = -1.28 \text{ eV}$ . For graphene, and using a  $k$ -point sampling of  $25 \times 25 \times 1$  we obtained a lattice constant  $a = 2.468 \text{ \AA}$ . This is slightly larger than values obtained by local density approximation<sup>38</sup> but is identical to a previous calculation using GGA.<sup>39</sup> The energy per carbon atom in graphene we obtained is  $E = -9.23 \text{ eV}$ .

Nudged elastic band (NEB) calculations<sup>40</sup> were per-

TABLE I. Interlayer relaxations in the slabs of Fig. 1 as percentage of the bulk distances.  $d_{ij}$  is the distance between layers  $i$  and  $j$ .

$d_{12}$	$d_{23}$	$d_{34}$	$d_{45}$	$d_{56}$	$d_{67}$	
(110)						
-0.1	0.3	-0.5	-0.2	0.04	0.2	Ref. 16
-0.11	1.16	1.14				Ref. 15
-0.4	0.5	-0.7				This work
(100)						
-3.6	2.3	0.4	-0.4	-0.01	-0.5	Ref. 16
-3.09	2.83	1.93				Ref. 15
-1.2	3.4	3.5				This work
(111)						
-17.7	-8.4	11.0	-1.0	-0.5	0.1	Ref. 16
-6.74	-16.89	12.4				Ref. 15
-3.8	-18.0	11.0	0.0	-0.7	1.6	This work

formed with VASP. Atoms in the topmost layer were allowed to move freely, and in some cases, the atoms below the topmost layer were allowed to move into  $z$  direction (normal to surface) only. Thus we were able to avoid the (artificial) collective movement of the surface slab atoms that sometimes occurred during the minimization.

### III. RESULTS

#### A. Morphology of $\alpha$ -iron facets

We can expect from some earlier studies concerning carbon solution into bulk iron and adsorption on iron surfaces,<sup>17,29</sup> that carbon prefers sites of maximum coordination: in bulk iron, it prefers the sixfold octahedral site<sup>29</sup> and on the (110) and (100) facets, carbon moves into sites that offer highest possible number of iron neighbors.<sup>17</sup> Keeping this in mind, we will give in this section a qualitative picture of carbon adsorption on different facets. This analysis is based on the octahedral site of bulk  $\alpha$ -iron.

The local coordination of the octahedral site is illustrated in Fig. 2(a). When carbon is adsorbed into this site, a tetragonal distortion in the bcc lattice takes place and distance B is expanded. As the bulk is cleaved along a specific direction in

order to create a surface, the octahedra become cleaved in a specific way, exposing octahedral sites. The way the octahedral sites are exposed in different facets, has been illustrated in Figs. 2(b)–2(d). On the (110) surface, the exposed octahedral sites have neighboring iron atoms at distances A and B. In the case of the (100) surface, there are several exposed octahedral sites where the neighboring iron atoms are simply at a distance A.

Assuming that carbon tries to maximize its coordination with iron on the surface (as discussed above), it will always prefer an exposed octahedral site, as this kind of site offers maximum coordination within the bcc lattice. The displacements of iron atoms surrounding a surface exposed octahedral should be very similar to the bulk tetragonal distortion [i.e., expansion of B and a slight contraction of A]. This distortion must be energetically very different on the distinct surfaces. Depending on how the distortion of A and B fits the facet morphology, quite different adsorbate-adsorbate repulsions can be formed; for example, expanding B on the (110) facet [Fig. 2(b)] consists of pushing neighboring iron atoms apart. On the (100) facet there are many sites with no significant need to rearrange the iron atoms as only small contraction of A is needed.

TABLE II. Magnetic moment of atoms in different layers ( $\mu_B$ ) in the slabs of Fig. 1. Number 1 denotes the bottom layer.

	1	2	3	4	5	6
110	2.57	2.28	2.17	2.17	2.29	2.56
100	2.96	2.37	2.47	2.50	2.38	2.96
111	1	2	3	4	5	6
	2.89	2.39	2.49	2.30	2.28	2.15
	7	8	9	10	11	12
	2.20	2.24	2.29	2.46	2.29	2.84



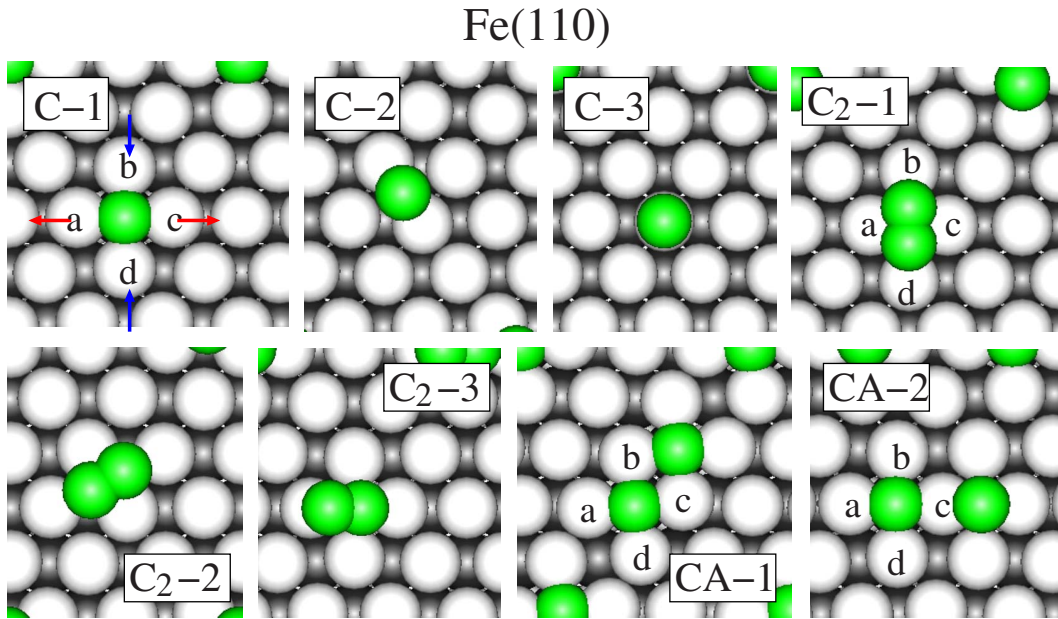


FIG. 3. (Color online) Some of the most stable geometries for C and C<sub>2</sub> on the Fe(110) surface. Different geometries are tagged with the same labels as in Table III. Coadsorption geometries, where atoms are adsorbed into the same unit cell are tagged with the label CA. Iron atom displacements upon carbon adsorption in (C-1) have been marked with arrows. These can be related to Fig. 2. In (CA-2) one adsorbed carbon atom is pushed toward vacuum.

**B. Bulk  $\alpha$ -iron facets**

For the bulk iron lattice constant we obtained  $a=2.83 \text{ \AA}$ , which agrees well with an earlier computational value<sup>29</sup> and the experimental value of  $2.87 \text{ \AA}$ .<sup>41</sup> For the bulk magnetic moment we obtained  $M=2.18 \mu_B$ . In earlier works, interlayer relaxations for various  $\alpha$ -iron facets have been studied.<sup>15,16</sup> The most important effect is the inward relaxation of the outermost layer. The interlayer relaxations can be sensitive to the slab size and to the scheme used (symmetric/

nonsymmetric slab, number of fixed layers).<sup>15,16</sup> In Table I we compare our results with previous ones. In our scheme, the slab is nonsymmetric as the atoms in the three bottom layers are fixed. There are then three topmost layers of freely relaxing atoms for (110) and (100), and nine for (111). This is similar to Ref. 15, where three topmost layers were allowed to relax while in Ref. 16 freestanding slabs were considered.

As evident from Table I we can see that the type of relaxation (either expansion or contraction) is quite consistent.

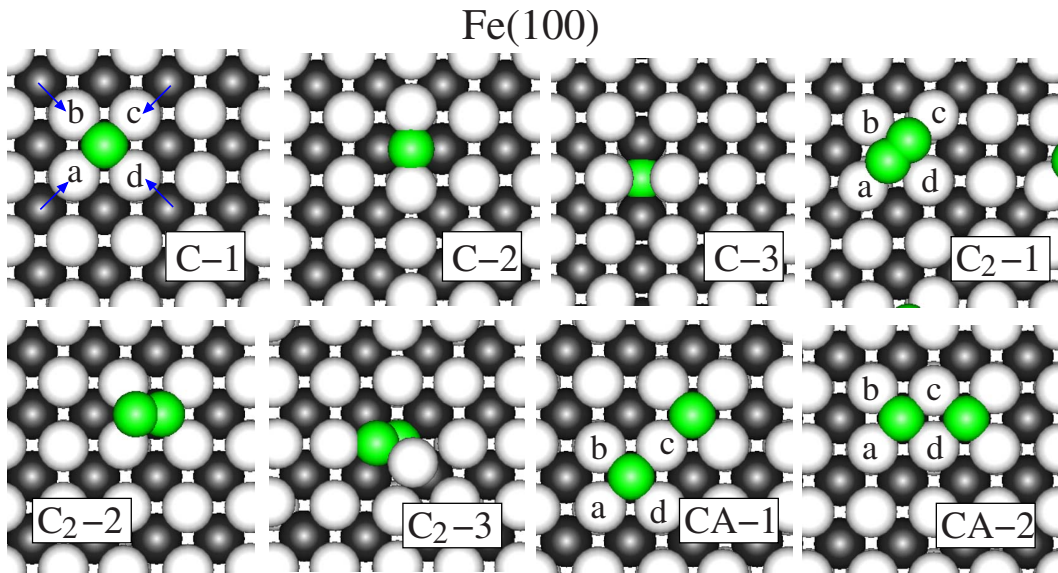


FIG. 4. (Color online) Some of the most stable geometries for C and C<sub>2</sub> on the Fe(100) surface. Different geometries are tagged with the same labels as in Table III. Coadsorption geometries, where atoms are adsorbed into the same unit cell are tagged with the label CA. Iron atom displacements upon carbon adsorption in (C-1) have been marked with arrows. These can be related to Fig. 2.

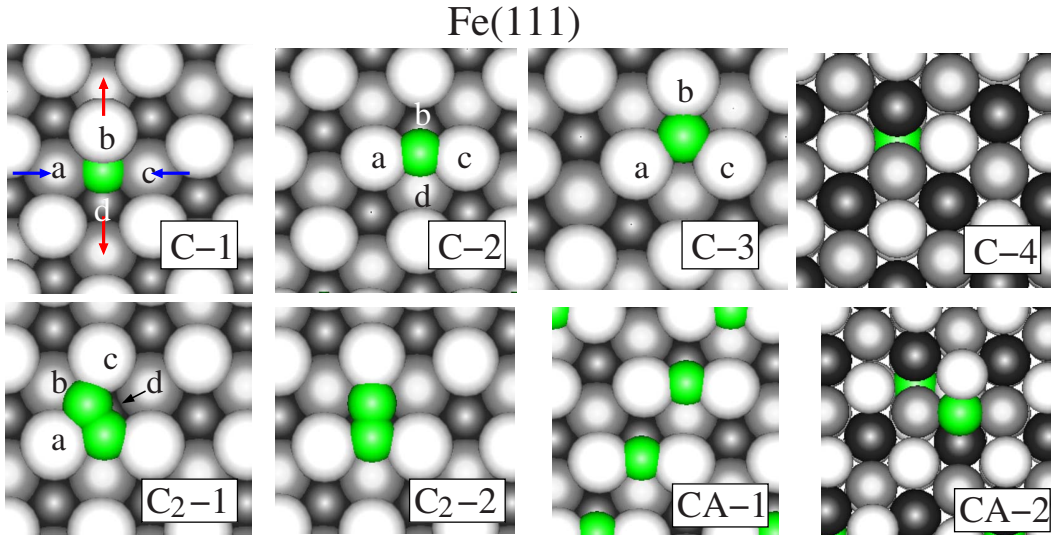


FIG. 5. (Color online) Some of the most stable geometries for C and  $C_2$  on the Fe(111) surface. Different geometries are tagged with the same labels as in Table III. Coadsorption geometries, where atoms are adsorbed into the same unit cell are tagged with the label CA. Iron atom displacements upon carbon adsorption in (C-1) have been marked with arrows. These can be related to Fig. 2.

The maximum differences in the top layer relaxations are of the order of 4 between our values and earlier computed values, but on the other hand, the absolute values are quite small; the interlayer distances in the bulk are approximately 2.00, 1.42, and 0.82 Å for the (110), (100), and (111) layers. The biggest absolute differences in  $d_{12}$  between our values and Ref. 16 (which we take as a benchmark) are then 0.006, 0.03, and 0.1 Å for the (110), (100), and (111) surface. We believe this is good enough for qualitative calculations. However, for high-precision quantitative calculations, thicker slabs should probably be used, especially for the Fe(111) surface.

Values of magnetic moment in different layers are presented in Table II. Consistent with earlier results<sup>16</sup> we observe that (100) has the highest top-layer magnetic moment and that in all slabs, the value of magnetic moment approach to that of bulk as we move inside the slab. Our values for the moments in the topmost layer,  $2.56 \mu_B$  (110),  $2.96 \mu_B$  (100), and  $2.84 \mu_B$  (111), compare well with the values of Ref. 16, namely,  $2.59 \mu_B$  (110),  $2.95 \mu_B$  (100), and  $2.81 \mu_B$  (111).

### C. Atomic carbon, coadsorption, and dimers

In this section we study atomic carbon adsorption [1/9  $\approx$  0.11 ML coverage for (110) and (100) and 1/4=0.25 ML coverage for (111)] as well as  $C_2$  dimer and carbon coadsorption. We study in detail how the adsorbates either repel or attract neighboring iron atoms in the topmost iron layers and will use the resulting displacements of iron atoms as our leading argument when describing the energetics at higher carbon concentrations in the next section.

#### 1. Atomic carbon

Adsorption geometries for carbon atoms (C-1, C-2, etc.) on the different facets are illustrated in Figs. 3–5. Corre-

sponding energetics are tabulated in Table III.

Look at Figs. 3–5, we can see that carbon favors the exposed octahedral sites of Fig. 2 as discussed in Sec. III A. The most favorable (C-1) sites for (110) and (100) are consistent with previous calculations.<sup>6,17,20,22</sup> From Table III the adsorption energies are  $-7.98$  eV and  $-8.45$  eV for the (110) and (100) surfaces, respectively. These compare well with earlier computed values of  $-7.92$  eV (Ref. 17) and  $-7.97$  eV (Ref. 6) for (110) and with  $-8.33$  eV,<sup>17</sup>  $-8.335$  eV (Ref. 20) for the (100) surface at the 0.11 ML concentration.

The iron atom directly below the adsorbed carbon atom in 100/C-1 shifts downwards, corresponding to expansion of B in Fig. 2. The coordination of carbon on (100) is fivefold<sup>17,20</sup> and it is bonded to the iron atom below at a distance of 1.98 Å. In the following we analyze in more detail the intralayer relaxations in the topmost surface layer, using as a guide the qualitative discussion of these relaxations made in Sec. III A; this kind of analysis, based on the tetragonal distortion of bulk adsorption, was made to some extent in Ref. 17, but only for the case of subsurface adsorption.

In 110/C-1 of Fig. 3 there are considerable intralayer relaxations in the topmost layer. The distance between iron atoms (b) and (d) contracts by 5% (0.20 Å, corresponding to contraction of A in Fig. 2) while the distance between (a) and (c) expands 23% (0.65 Å, corresponding to expansion of B). In 100/C-1 of Fig. 4 the displacement of iron atoms is smaller: now both distances (bd) and (bc) contract by 5% (0.15 Å), corresponding simply to the slight contraction of A; due to the specific cleaving of the octahedron in Fig. 2, the Fe(100) surface offers exposed octahedral sites for carbon with little need to arrange the surrounding iron atoms.

From Table III we can see that adsorption into 100/C-1 is 0.47 eV more favorable than adsorption into 110/C-1 (similar to the value of 0.41 eV obtained in Ref. 17). When looking at energies  $E_c$ , we observe that at a low coverage of 1/9 ML (i.e., single adsorbed atom), it is more favorable for the car-

TABLE III. Adsorption energies  $E_{ads}$  [see Eq. (2)], energies  $E_c$  [see Eq. (3)], and shifted energies  $E_s$  [see Eq. (1)]. Values of  $E_s$  can be used directly to calculate reaction energies on the surface by using Eq. (5). Values for C atoms and  $C_2$  molecules in different adsorption geometries on the  $\alpha$ -iron (110), (100), and (111) surfaces have been tabulated. Bond lengths (BL) for adsorbates and in vacuum (in parenthesis) are listed. In the last column the (mean) Bader electron occupations for carbon atom(s) ( $\bar{Q}_b$ ) have been tabulated (only valence electrons are considered; for an isolated carbon atom  $\bar{Q}_b=4.0$ ). Sites and geometries have the same labels as in Figs. 3–5 and in Table IV. Coadsorption geometries are tagged with the label “CA.”

Adsorbate	$E_{ads}$ (eV)	$E_c$ (eV)	$E_s$ (eV)	BL (Å)	$\bar{Q}_b$
Fe(110)					
C-1 (0.11 ML)	-7.98	-0.03	-9.26		5.4
C-2	-6.91	1.04	-8.19		5.0
C-3	-5.48	2.47	-6.76		4.6
$C_2$ -1 (0.22 ML)	-8.19	0.73	-17.72	1.35 (1.31)	5.2
$C_2$ -2	-8.04	0.88	-17.57	1.38	4.8
$C_2$ -3	-7.12	1.81	-16.64	1.32	4.7
CA-1 (0.22 ML)		0.2	-18.26		5.3
CA-2		0.74	-17.71		5.2
Fe(100)					
C-1 (0.11 ML)	-8.45	-0.50	-9.73		5.5
C-2	-7.2	0.74	-8.48		5.2
C-3	-7.18	0.77	-8.46		5.5
$C_2$ -1 (0.22 ML)	-8.26	0.67	-17.79	1.33	5.5
$C_2$ -2	-7.91	1.01	-17.44	1.36	4.8
$C_2$ -3	-7.51	1.42	-17.03	1.44	5.0
CA-1 (0.22 ML)		-1.02	-19.48		5.5
CA-2		-0.92	-19.38		5.4
Fe(111)					
C-1 (0.25 ML)	-7.74	0.20	-9.02		5.4
C-2	-7.69	0.26	-8.96		5.3
C-3	-7.43	0.52	-8.71		5.2
C-4	-7.41	0.53	-8.69		5.6
$C_2$ -1 (0.5 ML)	-8.95	-0.02	-18.47	1.40	4.9
$C_2$ -2	-8.87	0.05	-18.4	1.38	4.9
CA-1 (0.5 ML)		0.61	-17.84		5.3
CA-2		0.82	-17.63		5.5

bon atom to be adsorbed into the iron surface than to be incorporated into graphene. While in the case of (110), this tendency is very weak (only  $\sim 30$  meV), for (100) it is more significant (0.5 eV). As will be discussed below,  $E_c$  is very sensitive to the amount of carbon adsorbed on the facets: at lower concentrations than we are considering in this paper (less than  $1/9$  ML),  $E_c$  should become clearly negative also for (110).

The remaining adsorption geometries for (110), i.e., 110/C-2 and 110/C-3 are metastable down to  $\approx 0.012$  meV/Å and they lie more than 1 eV higher in energy than 110/C-1. Their characteristics (local minimum, higher order saddle point, etc.) have been discussed in more detail in Ref. 17. The energy values reported for the metastable adsorption ge-

ometries are approximative as their stabilization needs higher force tolerance in the calculations.

Comparing Fig. 2(d) and the optimal adsorption sites of carbon atoms in Fig. 5 we can see that carbon prefers exposed octahedral sites on the (111) facet. In 111/C-1, there is a 0.74 Å expansion in the distance of atoms (b-d) and a 0.2 Å contraction in the distance of atoms (a-c), corresponding again to B and A in Fig. 2(a). While adsorbate 111/C-2 exhibits very similar distortions, 111/C-3 breaks the trend a bit as it does not adsorb into an exposed octahedral site. It finds a high coordination by moving atoms (a), (b), and (c) instead. Atoms (a), (b), and (c) all move symmetrically  $\sim 0.3$  Å and their distance to the carbon atoms becomes 2.1 Å. There is also one iron atom directly below the carbon

TABLE IV. Reaction energies for forming  $C_2$  dimers and for bringing carbon atoms into coadsorption configurations. Geometries are tagged with the same labels (C-1, C-2, etc.) as in Table III and Figs. 3–5. Reaction energies are calculated by taking the corresponding energies  $E_s$  from Table III and applying Eq. (5).

Fe(110)		Fe(100)		Fe(111)	
Reaction	$\Delta E$	Reaction	$\Delta E$	Reaction	$\Delta E$
$2(C-1) \rightarrow C_2-1$	0.79	$2(C-1) \rightarrow C_2-1$	1.67	$2(C-1) \rightarrow C_2-1$	-0.42
$2(C-2) \rightarrow C_2-1$	-1.35	$2(C-2) \rightarrow C_2-1$	-0.82	$2(C-2) \rightarrow C_2-1$	-0.54
$(C-1)+(C-2) \rightarrow C_2-1$	-0.28	$(C-1)+(C-2) \rightarrow C_2-1$	0.43	$(C-1)+(C-2) \rightarrow C_2-1$	-0.48
$CA-1 \rightarrow C_2-1$	0.53	$CA-1 \rightarrow C_2-1$	1.69	$CA-1 \rightarrow C_2-1$	-0.63
$CA-2 \rightarrow C_2-1$	-0.01	$CA-2 \rightarrow C_2-1$	1.59	$CA-2 \rightarrow C_2-1$	-0.84
$2(C-1) \rightarrow CA-1$	0.26	$2(C-1) \rightarrow CA-1$	-0.02	$2(C-1) \rightarrow CA-1$	0.21
$2(C-1) \rightarrow CA-2$	0.81	$2(C-1) \rightarrow CA-2$	0.08	$2(C-1) \rightarrow CA-2$	0.41

at a distance of 1.85 Å. Adsorbate 111/C-4 is simply a carbon atom adsorbed at a bulklike octahedral site.

When looking at the adsorption geometry C-1, we see that it is by definition a “subsurface” site, i.e., the carbon atom resides below the topmost iron layer. On the other hand, it has not yet obtained a coordination with surrounding iron atoms similar to that in bulk. On the contrary, C-2 is clearly a “surface” adsorption site. The energy difference between C-1 (a “semi” subsurface site) and C-2 (“surface” site) is minimal, only 50 meV.

The energetics for carbon adsorption on (111) in Table III are not directly comparable to those reported in Ref. 6, as in that work the movement of iron atoms was constrained (some of the sites will have different local geometries upon relaxation). Our values for the C-1 (-7.74 eV) and C-3 (-7.43 eV) sites are very close to the value reported in Ref. 6 (-7.60 eV) for a similar site.

Finally, the Bader occupation of carbon atoms in the different adsorption geometries have been tabulated in the last row of Table III. Carbon atoms in bulklike sites, such as 100/C-3 and 111/C-4 obtain the highest occupation with approx. 1.5 extra electrons. The most favorable top layer adsorption sites, i.e., the “C-1” adsorbates, have typically higher Bader occupation than the remaining geometries. Carbon seems to prefer high coordinated sites that provide a high number of electrons. For example, the site 100/C-1 is optimal because it (a) provides a high number of electrons (1.5 extra electrons) and (b) there is no need to rearrange the surrounding iron atoms in order to fit into this site (as discussed earlier in this section).

## 2. $C_2$ dimer

Assuming that carbon atoms in the dimer prefer similar high-coordinated sites as the individual atoms while maintaining a reasonable carbon-carbon bond length, there are not good possibilities to achieve this on the (110) and (100) surfaces, as the optimal C-1 sites lie far away from each other. The case of (111) is very different; looking at Fig. 2(d) we can see that there is an abundance of optimal adsorption sites within the bond length of a carbon dimer. We can then expect that  $C_2$  dimer is most stable on the (111) surface.

The optimal  $C_2$  adsorption geometries on the (110) and (100) of Figs. 3 and 4 are in both facets quite similar: individual carbon atoms are onefold to threefold coordinated to iron: one Fe-C distance in both cases is 1.85 Å while the remaining two Fe-C distances are  $\approx 2.0$  Å. The C-C bond length for 110/ $C_2-1$  is slightly expanded while for 100/ $C_2-1$  it is closer to the isolated  $C_2$  bond length. In 110/ $C_2-1$ , both iron atom distances ac and bd expand by  $\sim 5\%$  while in 100/ $C_2-1$ , the distance between a and c is expanded by  $\sim 15\%$ . Of the remaining  $C_2$  adsorption geometries 110/ $C_2-2$  exhibits similar trend as  $C_2-1$ : both C atoms reside in a site which is approx. threefold to iron atoms. Other  $C_2$  adsorption geometries are trying to adopt positions where the adsorbed carbon can reside in C-1, C-2, or C-3 sites

The optimal position,  $C_2-1$  for the carbon dimer on (111) is depicted in Fig. 5. Both carbon atoms reside in a C-1 site while the Fe-C distances are  $\approx 2$  Å. The C-C length in the dimer is expanded by  $\approx 6\%$ . The adsorbate  $C_2-2$  exhibits a similar trend. Comparing the adsorption energies of  $C_2-1$  in the case of the different facets (Table III), the adsorption of the carbon dimer on 111 is at least  $\approx 0.7$  eV more favorable than on the other facets; as discussed above, this is because the (111) facet offers nearby optimal adsorption sites for the carbon atoms.

The reaction energetic of Table IV further demonstrate that it is much more favorable to form carbon dimers on the (111) facet than on the (110) and (100) facets. The (100) facet favors less dimer formation than the other ones, as having carbon in atomic form is energetically so favorable on this facet.

## 3. Coadsorption

We have studied coadsorption configurations by placing two carbon atoms in a sublattice of the most optimal adsorption sites of the individual carbon atoms. The optimal coadsorption sites we found are marked with tags “CA” in Figs. 3–5.

In the case of (110) (Fig. 4) the two coadsorption configurations considered become very different; in 110/CA-1, both carbon atoms reside in a 110/C-1 adsorption site. However, in 110/CA-2, one of the carbon atoms is forced to move from the C-1 site toward vacuum. As discussed earlier, this results



$N_C$	$N_{conf}$	$E_c$ (eV)	$\bar{Q}_b$ ( $e^-$ )	$N_C$	$N_{conf}$	$E_c$ (eV)	$\bar{Q}_b$ ( $e^-$ )
1	1	-0.5	5.5	6	4	-2.56	5.4
2	2	-1.02	5.5	7	2	-1.65	5.4
3	4	-1.26	5.4	8	1	-0.12	5.3
4	5	-1.49	5.4	9	4	1.85	5.2
5	5	-2.27	5.4	9		$C^* + C^* \rightarrow C_2^*$ : $\Delta E = -1.10$ eV	

FIG. 6. (Color online) Adsorption geometries where carbon atoms are adsorbed in the sublattice formed by the C-1 sites (see Fig. 4).  $N_C$  is the number of carbon atoms and  $N_{conf}$  the number of all possible coadsorption configurations when  $N_C$  atoms are adsorbed on a  $(3 \times 3)$  C-1 sublattice. For a particular coadsorption geometry illustrated in the table, energy  $E_c$  and the mean Bader electron occupations for carbon atoms ( $\bar{Q}_b$ ) have been tabulated (for an isolated carbon atom  $\bar{Q}_b = 4.0$ ). Displacements of some iron atoms upon carbon adsorption have been highlighted by blue arrows. In the last row and column, the energy gain when forming a  $C_2$  molecule at the 1 ML concentration is calculated.

from the expansion of distance B (Fig. 2) on the (110) facet; in 110/C-1, atoms (a) and (c) are pushed apart and in 110/CA-2 the carbon atoms are pushing the same atom (c) into opposite directions. This creates strong repulsion between the carbon atoms and only one can be accommodated into the C-1 site. This results in a notable, 0.5 eV energy difference between configurations 110/CA-1 and 110/CA-2.

The situation is very different on the (100) surface. As discussed above, the adsorption of carbon to the 100/C-1 site does not involve considerable motion of the surface iron atoms, as the only displacement needed is the very small contraction of A (Fig. 2). In the optimal coadsorption geometries 100/CA-1 and 100/CA-2 of Fig. 4 there are indeed very minor displacements of iron atoms toward the adsorbed carbon. In CA-2 both carbon atoms attract iron atoms (c) and (d) while in CA-1 they pull only one common iron atom (c). In Table III we can see that this results in a small 0.1 eV energy difference between CA-1 and CA-2.

In the case of the (111) surface, there are quite many neighboring optimal adsorption sites (C-1 and C-2) and so the number of coadsorption configurations becomes large. The two most optimal configurations we found (CA-1 and CA-2) are illustrated in Fig. 4.

#### D. Higher carbon concentrations

In this section, we study the effect of high carbon concentrations [ $>2/9$  ML for (110) and (100),  $>3/4$  ML for (111)]

on energies  $E_c$  [Eq. (3)]. Carbon is adsorbed on the sublattice formed by the most favorable C-1 adsorption sites. Our study is most systematic for the (100) surface as there is an obvious way how to place an increasing number of carbon atoms on the surface: we do not expect considerable displacement of iron atoms from the bulk positions nor movement of carbon atoms away from the optimal C-1 adsorption sites. On the other hand, as we saw in previous sections, on (110) surface adsorbed carbon atoms start to repel each other while on (111) we can expect dimer formation. Our objective for (110) and (111) is simply to further demonstrate these points (adsorbate repulsion, dimer formation) at higher carbon concentrations. We start with the case we studied most systematically, i.e., with the (100) surface.

*(100) surface.* Carbon concentrations of up to 1 ML have been considered for the (100) facet in Fig. 6. A minimum of energy  $E_c$  as function of carbon concentration occurs at the coverage of  $6/9 \approx 0.667$  ML at an adsorption configuration “ $3\sqrt{(2)} \times \sqrt{(2)}$ .” This configuration was first reported in a combined theoretical and experimental study by Panaccione *et al.* in Ref. 19, and later studied theoretically by Trimarchi and Binggeli,<sup>21</sup> followed by Tan *et al.*<sup>20</sup> In the  $3\sqrt{(2)} \times \sqrt{(2)}$  configuration, carbon atoms form an infinite zigzag wire on the C-1 sublattice. There exists even more favorable coadsorption configuration “ $c(2 \times 2)$ ” which is observed at the coverage of 0.50 ML.<sup>18,17,20</sup> Both of these stable structures have been analyzed using scanning tunnel microscope and/or

low-energy electron diffraction<sup>18,19</sup> For the  $6/9$  ML  $3\sqrt{(2)} \times \sqrt{(2)}$  coadsorption structure presented in Fig. 6 we observe similar atomic movements as reported in earlier studies,<sup>19–21</sup> most notably the displacements of iron atoms in the topmost layer as illustrated schematically in Fig. 6.

A very interesting phenomena in the case of the (100) surface is the behavior of  $E_c$  in Fig. 6 as function of carbon concentration: the system gains in stability as more carbon is adsorbed on the surface. At concentrations greater than  $6/9$  ML, the system starts to loose this energy gain while at 1 ML it becomes more favorable to place carbon atoms in graphene than adsorb them on the surface. This behavior can be explained by considering the displacements of iron atoms in the topmost surface layer.

From the reconstruction patterns presented by arrows in Fig. 6 we can see that iron atoms move always toward the adsorbed carbon. These changes in iron atom positions are typically in the range of  $\sim 0.2$ – $0.3$  Å (in accordance what was discussed in Secs. III C 1 and III C 3). As carbon concentration increases, iron atoms become increasingly “frustrated” as they are surrounded by carbon; at 1 ML coverage, an iron atom has so many neighboring carbon atoms that it cannot obtain optimal bonding conditions with any of them.

This frustration mechanism results in sudden change in the energetics of the (100) facet; even at such a high concentration as  $8/9$  ML, it is more favorable to adsorb carbon atoms to the C-1 sublattice than incorporate them into graphene, but when going from  $8/9$  ML to 1 ML, this tendency is suddenly reversed. In the last row and column of Fig. 6, we present the energy gain when releasing this “surface frustration” by dimer formation. It is quite large, over 1 eV.

*(110) surface.* Some configurations of carbon for up to 1 ML have been considered for the (110) facet in Fig. 7. The initial configurations consisted of adsorbing carbon atoms on either the C-1, C-3, or C<sub>2</sub>-1 sublattice (see Fig. 3) and the final, relaxed geometries are presented in Fig. 7. As we discussed in Sec. III C 3, at  $2/9$  ML coverage there are coadsorption configurations where carbon adsorbates start to repel each other. Such effects become more important at higher carbon concentrations. In Fig. 7 and for a  $3/9$  ML concentration, there is still one possibility to adsorb carbon without creating an excess of surface stress, similar to CA-1 of Fig. 3 and this is illustrated in the stringlike configuration of C3–1. If we place atoms at the same  $3/9$  ML concentration to a C-3 sublattice, only one carbon atom is adsorbed into a C-1 site and the remaining atoms form spontaneously a dimer. This is demonstrated in configuration C3–2 of Fig. 7.

At  $4/9$  ML coverage we have considered several different configurations: C4–1 is very similar to CA-2 of Fig. 4 and the surface stress is again released by expelling two atoms toward vacuum while maintaining at least two other atoms on the C-1 site; in C4–4, a complex reconstruction, where all carbon atoms are residing in threefold adsorption sites occurs; at  $6/9$  ML concentration, even iron atoms are expelled from the surface in order to release surface strain and to accommodate carbon atoms in the C-1 site; in C6–2, a C-Fe-C molecule is spontaneously formed.

*(111) surface.* In the case of the (111) we discussed how there is an abundance of open octahedral sites (C-1 and C-2

$N_C$		$E_c$ (eV)	$N_C$		$E_c$ (eV)
3	C3-1	0.74	4	C4-3	2.13
3	C3-2	1.34	4	C4-4	3.1
4	C4-1	1.72	6	C6-1	2.52
4	C4-2	1.77	6	C6-2	3.29

FIG. 7. (Color online) Relaxed adsorption geometries on (110) after carbon atoms have been placed in a sublattice formed by the C-1 (C3–1, C4–1, C6–2), C-3 (C3–2, C4–4, C6–1) and C<sub>2</sub>-1 (C4–2, C4–3) configurations of Fig. 3. Number of carbon atoms per unit cell ( $N_C$ ) and energies  $E_c$  have been tabulated.

in Fig. 5). We also pointed out that these sites are close to each other so that C<sub>2</sub> dimers are naturally formed. Some of the most favorable coadsorption configurations at higher concentrations on the (111) surface have been illustrated in Fig. 8. From the energetics in Fig. 8, we see that there is an energy cost when adsorbing more carbon on the surface but not as high as in the case of (110); no strong repulsion of carbon atoms takes place as there are plenty of adsorption sites and the top layer atoms in (111) are flexible to move. In (110), the C<sub>2</sub> dimers were formed above the topmost surface, resulting from expulsion of carbon atoms from the C-1 sites,

$N_C$		$E_c$ (eV)	$N_C$		$E_c$ (eV)
3	C3-1	1	5	C5	0.46
3	C3-2	1.36	6	C6	0.93
4	C4	0.95	7	C7	0.56

FIG. 8. (Color online) Relaxed adsorption geometries on (111) after carbon atoms have been placed in a sublattice formed by the C-1 and C-2 sites (see Fig. 5). Number of carbon atoms per unit cell ( $N_C$ ) and energies  $E_c$  have been tabulated.

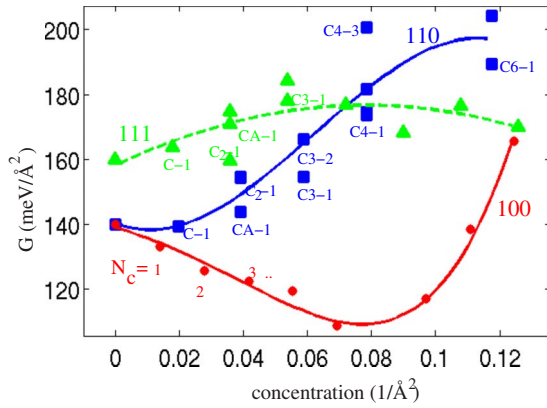


FIG. 9. (Color online) Surface energy  $G$  [Eq. (7)] as function of carbon coverage (atoms per  $\text{\AA}^2$ ) on the (110), (100), and (111) facets. Energies correspond to the fully relaxed adsorption geometries of Figs. 3–8. Energy at zero concentration has been fixed to the surface energy of the empty facet [140 meV/ $\text{\AA}^2$  for (110) and (100), 160 meV/ $\text{\AA}^2$  for (111)], as described by Eq. (7).

while in the (111), the carbon dimers are formed below the topmost layer, in the very same sites where the atomic carbon is adsorbed.

**Surface energies.** The energetics of Table III and Figs. 6–8 are also shown in Fig. 9 as surface energies [employing Eq. (7)]. This figure is not to be taken as an exact representation of surface energies as function of carbon concentration; situations with “graphenated” surfaces (see Ref. 6) and many possible carbon adsorption configurations are missing. However, one can see some clear trends: the steep rise in the surface energy as function of carbon concentration in the (110) facet implies aggressive graphene formation on this facet; the (100) facet forms stable carbon rich phases near  $0.5 \text{ ML} = 0.081/\text{\AA}^2$ ; at high carbon concentrations the (111) facet gains in relative stability with respect to (100) facet. This stabilization can be understood in terms of frustration of the (100) facet, and from the bigger number of adsorption sites available and the flexibility of the topmost iron atoms on the (111) facet, as discussed above.

### E. Diffusion

Diffusion on and into the (110) and (100) facets has been calculated earlier by Jiang and Carter.<sup>17</sup> The “C-2” configurations in Figs. 3 and 4 constitute the transition states and one could obtain the energy barrier directly from the energy difference of C-2 (transition state) and “C-1” (minimum energy). As mentioned in Sec. I, it can be difficult to find with high precision the energy of a saddle point as the system tends to relax toward the energy minimum. We thus performed NEB calculations with five image points between C-1 configurations and this way obtained activation barriers  $E_a = 1.21 \text{ eV}$  and  $E_a = 1.46 \text{ eV}$  for the (110) and (100) surfaces, respectively. Jiang and Carter considered the activation barriers in a higher (0.25 ML) carbon coverage than in this work (0.11 ML) and obtained 0.96 eV and 1.45 eV, for the (110) and (100) surfaces, respectively. Keeping in mind the different adsorbate concentration, the agreement is quite

good; for the (100) facet an almost exact agreement while the barrier for the (110) facet in our case (and at lower concentration) is 0.25 eV higher. The lower diffusion barrier (0.96 eV) at higher carbon coverage (0.25 ML) on the (110) surface can be consistent with the ideas proposed in earlier chapters: at high carbon concentrations carbon atoms on the (110) facet are displaced slightly toward the vacuum where the diffusion barrier should be smaller.

Surface to subsurface diffusion on the (110) and (100) facets have been studied earlier by Jiang and Carter<sup>17</sup> and by Sorescu.<sup>22</sup> In this work we report results for carbon diffusion on and into the (111) facet which, to our knowledge, have not been calculated earlier using *ab initio* methods.

When studying subsurface adsorption and diffusion, one must keep in mind the deep interlayer relaxations of pure iron slabs and the elongation/contraction of distances  $A$  and  $B$  (Fig. 2) which might propagate far in the lattice. Then a thorough investigation of activation energies and energy cost for carbon atom to enter the bulk would require calculations with very thick slabs, considering increasing adsorption depths until bulk values are recovered. In Ref. 17 barriers and energetics for (110) and (100) were calculated down to the first subsurface layer while in Ref. 22 alternative diffusion route into the Fe(100) was proposed and minimum energy path down to the third subsurface layer was calculated.

As discussed in Sec. III C 1 for (111) facet, the 111/C-1 site of Fig. 5 can be classified as “semi” subsurface site. In our calculations, we have considered also the first “true” subsurface site (i.e., a site that has a octahedral bulklike coordination) but have not pursued the calculation of the diffusion barrier when going very deep inside the slab as the finite size of our slab might affect the results.

Carbon diffusion between neighboring C-2 sites and between the C-1 and C-2 sites is illustrated in Fig. 10(a). Diffusion from C-1 deeper into the slab and reaching a site “N” where carbon has similar coordination as in the bulk octahedral site, is illustrated in Fig. 10(b). This site with adsorption energy  $E_{ads} = -7.22 \text{ eV}$  should not be confused with the C-4 adsorbate of Fig. 5 which lies even deeper inside the slab [energy of C-4 is indicated in Fig. 10(b)].

The activation energy for surface diffusion between C-2 sites reported here ( $E_a = 1.12 \text{ eV}$ ) is of the same magnitude as the activation energy for surface diffusion on Fe(110) (i.e., 0.96–1.21 eV, see above) and smaller than on the Fe(100) surface (1.45 eV). According to Fig. 10(a), going from C-2 site to a neighboring semi subsurface site C-1 has a small barrier of 0.43 eV and from Fig. 10(b), going slightly deeper inside the slab to the N site, has a barrier of 0.77 eV. Carbon atoms on the Fe(111) surface can then move very easily between neighboring C-1 and C-2 sites ( $E_a = 0.43 \text{ eV}$ ) i.e., within the “triangle” formed by the topmost iron atoms. Moving from one triangle to another seems to be easier through the N geometry, which is in halfway between two C-1 sites (0.77 eV), than following the C-2  $\rightarrow$  C-2 path (1.12 eV) of Fig. 10(a).

As illustrated in the insets of Fig. 10(b), in the transition state of the minimum energy path, one atom in the topmost iron layer is pushed away from the carbon atom. However, the barrier is relatively small (0.77 eV) because the iron atoms in the (111) topmost layer are low coordinated and flex-



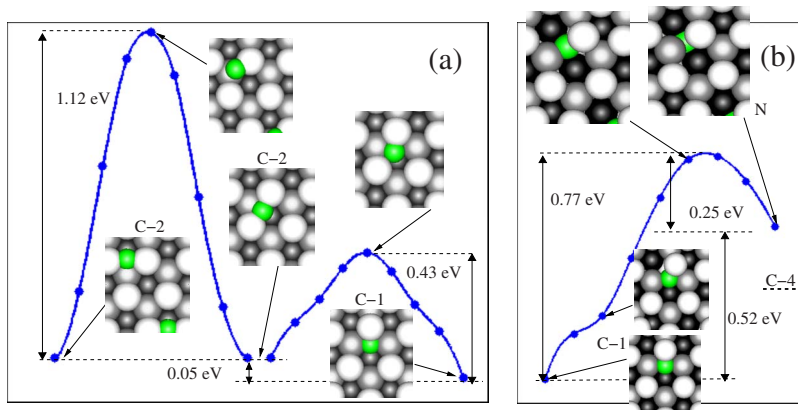


FIG. 10. (Color online) (a) Diffusion on (111) into the C-1 and C-2 sites (Fig. 4) and (b) into a deeper subsurface site (N). The energy of adsorbate “C-4” (Fig. 5) has been marked in panel (b) with a dashed line.

ible to move. We identify the 0.77 eV barrier tentatively as the activation energy for carbon atom to enter the surface and it is smaller than those reported for (110) [1.18 eV (Ref. 17)] and (100) [1.47 eV (Ref. 17) and 1.35 eV (Ref. 22)].

Apart from the activation barriers, the energy cost when going from surface to subsurface is quite different on the Fe(111) facet when comparing to (110) and (100): from Table III the energy cost of going from 111/C-1 to 111/C-4 is only 0.33 eV, which is smaller than on Fe(110) (0.62 eV) and Fe(100) [1.19 eV (Ref. 17) and 1.07 eV (Ref. 22)]. There are then clear indications that the exchange of carbon atoms between the topmost and deeper layers is easier on the (111) than on (110) and (100) facets.

#### IV. DISCUSSIONS AND CONCLUSIONS

This work was motivated by the recent *in situ* studies of carbon nanotube growth from “large” iron nanoparticles where different nanoparticle facets seem to behave in a very different manner. The facets studied in this work correspond to those identified in Ref. 6, namely, the  $\alpha$ -iron (110), (100), and (111) surfaces. We have studied the effect of adsorbing increasing amounts of carbon on these surfaces

The repulsion among adsorbed carbon atoms on the (110) facet is strong and because of this, carbon atoms are expelled from the optimal adsorption sites when carbon concentration is increased. This may happen already at the relatively low 0.22 ML concentration, resulting in dimer and graphene formation.

The (100) facet behaves in a very different way, as stable, carbon rich structures are formed near 0.5 ML concentration. When approaching 1 ML carbon concentration, (100) is destabilized due to frustration of the top layer iron atoms, which can be released by dimer and graphitic material formation.

The (111) surface behaves again in a distinct manner; the surface energy is rather insensitive to the amount of carbon adsorbed on it [at similar atoms/ $\text{\AA}^2$  concentrations where (100) becomes unstable]. This results from the abundance of adsorption sites and from the flexibility of the topmost iron atom layer.

Carbon nanotube and graphene formation are known to be highly kinetic processes so one must be cautious when relating the present work-based mainly on total energies of dif-

ferent adsorbed carbon concentrations—to these processes. However, the arguments concerning the nature of adsorbate repulsions and surface iron atom frustration on the different facets are valid also in a dynamical situation and at higher temperatures, as long as the nanoparticles are crystalline.

The sudden carbon “supersaturation” at the (100) facet near 1 ML carbon concentration might be related to the lift of graphitic caps from this facet as more carbon is injected into the nanoparticle as seen in the *in situ* experiment.<sup>6</sup> When carbon feedstock is exhausted in the experiment, the (111) facets start to shrink and eventually they disappear.<sup>6</sup> This is very likely related to our computational results: the relative stabilities of (100) and (111) were observed to be sensitive to the amount of adsorbed carbon. At low carbon concentration (100) gains in stability while at high concentrations, (111) becomes equally stable. The exchange of carbon between the topmost iron layer and the subsurface layers was seen to be easier on (111) than on the other facets. Carbon dimer formation was observed to be most favorable on (111). This could be related to a typical TEM image of a CVD grown multiwalled carbon nanotubes that show several graphitic layers emerging from the (111) facet.<sup>6</sup>

These last observations can be important when trying to understand the growth mechanisms of carbon nanotubes in general: in a pure  $\alpha$ -iron nanoparticle, the portion of (111) facets is very small.<sup>16</sup> As carbon concentration on the nanoparticle surface gets higher, (111) facets will be stabilized. Once these facets have been established, graphitic material growth from them can proceed as they favor  $C_2$  formation and as the movement of carbon atoms between subsurface and surface is easier. However, in order to make this idea more solid, more investigation about the diffusion of carbon and kinetics of graphene growth on the (111) facet must be performed.

To summarize, carbon concentrations at the monolayer range were studied on  $\alpha$ -iron facets. Such aspects as repulsion between carbon adsorbates on the (110) the frustration of iron atoms on the (100) surface and the dimer formation on (111) facet together with their effect on the surface energies were discussed. Diffusion on and into the (111) facet was studied. Our findings were related to a recent *in situ* study where the appearance of (111) facets correlates with increased carbon concentration. A general idea where increased carbon concentration stabilizes the (111) facets [with respect to (100) facets] followed by growth of graphitic material from these facets was proposed.



## ACKNOWLEDGMENTS

We wish to thank the Center for Scientific Computing, for use of its computational resources. This work has been supported in part by the European Commission under the

Framework Programme (STREP project BNC Tubes, Contract No. NMP4-CT-2006-03350) and the Academy of Finland through its Centre of Excellence Programme (2006-2011).

\*sampsariikonen@iki.fi

- <sup>1</sup>R. Sharma and Z. Iqbal, *Appl. Phys. Lett.* **84**, 990 (2004).
- <sup>2</sup>S. Helveg, C. Lopez-Cartes, J. Sehested, P. L. Hansen, B. S. Clausen, J. R. Rostrup-Nielsen, F. Abild-Pedersen, and J. K. Nørskov, *Nature (London)* **427**, 426 (2004).
- <sup>3</sup>S. Hofmann *et al.*, *Nano Lett.* **7**, 602 (2007).
- <sup>4</sup>K. Jensen, W. Mickelson, W. Han, and A. Zettl, *Appl. Phys. Lett.* **86**, 173107 (2005).
- <sup>5</sup>F. Abild-Pedersen, J. K. Nørskov, J. R. Rostrup-Nielsen, J. Sehested, and S. Helveg, *Phys. Rev. B* **73**, 115419 (2006).
- <sup>6</sup>G. E. Begtrup, W. Gannett, J. C. Meyer, T. D. Yuzvinsky, E. Ertekin, J. C. Grossman, and A. Zettl, *Phys. Rev. B* **79**, 205409 (2009).
- <sup>7</sup>J. A. Rodríguez-Manzo, M. Terrones, H. Terrones, H. W. Kroto, L. Sun, and F. Banhart, *Nat. Nanotechnol.* **2**, 307 (2007).
- <sup>8</sup>H. Yoshida, S. Takeda, T. Uchiyama, H. Kohno, and Y. Homma, *Nano Lett.* **8**, 2082 (2008).
- <sup>9</sup>J. A. Rodríguez-Manzo, I. Janowska, C. Pham-Huu, A. Tolvanen, A. V. Krasheninnikov, K. Nordlund, and F. Banhart, *Small* **5**, 2710 (2009).
- <sup>10</sup>R. Sharma, E. Moore, P. Rez, and M. M. J. Treacy, *Nano Lett.* **9**, 689 (2009).
- <sup>11</sup>H. S. Bengaard, J. K. Nørskov, J. Sehested, B. S. Clausen, L. P. Nielsen, A. M. Molenbroek, and J. R. Rostrup-Nielsen, *J. Catal.* **209**, 365 (2002).
- <sup>12</sup>A. R. Harutyunyan, N. Awasthi, A. Jiang, W. Setyawan, E. Mora, T. Tokune, K. Bolton, and S. Curtarolo, *Phys. Rev. Lett.* **100**, 195502 (2008).
- <sup>13</sup>A. S. Barnard and P. Zapol, *J. Chem. Phys.* **121**, 4276 (2004).
- <sup>14</sup>S. Hofmann, G. Csanyi, A. C. Ferrari, M. C. Payne, and J. Robertson, *Phys. Rev. Lett.* **95**, 036101 (2005).
- <sup>15</sup>P. Błoński and A. Kiejna, *Vacuum* **74**, 179 (2004).
- <sup>16</sup>P. Błoński and A. Kiejna, *Surf. Sci.* **601**, 123 (2007).
- <sup>17</sup>D. E. Jiang and E. A. Carter, *Phys. Rev. B* **71**, 045402 (2005).
- <sup>18</sup>V. Blum, A. Schmidt, W. Meier, L. Hammer, and K. Heinz, *J. Phys.: Condens. Matter* **15**, 3517 (2003).
- <sup>19</sup>G. Panaccione, J. Fujii, I. Vobornik, G. Trimarchi, N. Binggeli, A. Goldoni, R. Larciprete, and G. Rossi, *Phys. Rev. B* **73**, 035431 (2006).
- <sup>20</sup>X. Tan, J. Zhou, F. Liu, Y. Peng, and B. Zhao, *Eur. Phys. J. B* **74**, 555 (2010).
- <sup>21</sup>G. Trimarchi and N. Binggeli, *Phys. Status Solidi B* **243**, 2105 (2006).
- <sup>22</sup>D. C. Sorescu, *Phys. Rev. B* **73**, 155420 (2006).
- <sup>23</sup>W. C. Chiou and E. A. Carter, *Surf. Sci.* **530**, 88 (2003).
- <sup>24</sup>R. J. D. Tilley, *Understanding Solids: The Science of Materials* (Wiley, 2004).
- <sup>25</sup><http://en.wikipedia.org/wiki/Steel>
- <sup>26</sup>G. Rollmann, M. E. Gruner, A. Hucht, R. Meyer, P. Entel, M. L. Tiago, and J. R. Chelikowsky, *Phys. Rev. Lett.* **99**, 083402 (2007).
- <sup>27</sup>A. Postnikov, P. Entel, and J. Soler, *Eur. Phys. J. D* **25**, 261 (2003).
- <sup>28</sup>J. P. Perdew, K. Burke, and M. Ernzerhof, *Phys. Rev. Lett.* **77**, 3865 (1996).
- <sup>29</sup>D. E. Jiang and E. A. Carter, *Phys. Rev. B* **67**, 214103 (2003).
- <sup>30</sup>A. S. Barnard and P. Zapol, *Phys. Rev. B* **70**, 235403 (2004).
- <sup>31</sup>J. C. Boettger, *Phys. Rev. B* **53**, 13133 (1996).
- <sup>32</sup>G. Kresse and J. Furthmüller, *Phys. Rev. B* **54**, 11169 (1996).
- <sup>33</sup>G. Kresse and D. Joubert, *Phys. Rev. B* **59**, 1758 (1999).
- <sup>34</sup>P. E. Blöchl, *Phys. Rev. B* **50**, 17953 (1994).
- <sup>35</sup>H. J. Monkhorst and J. D. Pack, *Phys. Rev. B* **13**, 5188 (1976).
- <sup>36</sup>S. Riikonen, A. S. Foster, A. V. Krasheninnikov, and R. M. Nieminen, *Phys. Rev. B* **80**, 155429 (2009).
- <sup>37</sup>M. Methfessel and A. T. Paxton, *Phys. Rev. B* **40**, 3616 (1989).
- <sup>38</sup>L. Wirtz and A. Rubio, *Solid State Commun.* **131**, 141 (2004).
- <sup>39</sup>G. Gui, J. Li, and J. Zhong, *Phys. Rev. B* **78**, 075435 (2008).
- <sup>40</sup>G. Henkelman, B. P. Uberuaga, and H. Jónsson, *J. Chem. Phys.* **113**, 9901 (2000).
- <sup>41</sup>C. Kittel, *Introduction to Solid State Physics*, 6th ed. (Wiley, New York, 1986).